INTERFACE SCIENCE, 2, 211–220 (1994)

Atomic Structure and Electronic Properties of the Σ37(610) and Σ29(520) [001] Tilt Grain Boundaries in Ge *

S. RUVIMOV
Max Planck Institute of Microstructure Physics, D-06120 Halle, Germany
A.F. Ioffe Physical Technical Institute, 194021 St. Petersburg, Russia

J. HEYDENREICH, R. SCHOLZ AND K. SCHEERSCHMIDT
Max Planck Institute of Microstructure Physics, D-06120 Halle, Germany

N.I. BOCHKAREVA AND L.M. SOROKIN
A.F. Ioffe Physical Technical Institute, 194021 St. Petersburg, Russia

Abstract. 400 kV high resolution electron microscopy (HREM), deep level transient spectroscopy (DLTS) and steady state electrical measurements have been applied to Σ37(610) and Σ29(520) [001] tilt grain boundaries (GBs) in germanium bicrystals. The atomic boundary structures were revealed by experimental HREM images taken under different defocus conditions. Later, structure models were refined by means of a trial-and-error method applying alternatively the image simulation and the molecular static calculation of relaxed structures. The structures were shown to be consistent with the modified structural unit model. Although the structures are different for the two GBs studied, DLTS data and steady state measurements were found to be quite similar for both GBs. Thus, the results point to the extrinsic origin of localized deep states at the GBs. The analysis of DLTS spectra indicates the impurity segregation at the boundary, e.g., the formation of vacancy-type oxygen complexes of a donor-like state at E_c-0.21 eV, which results in the fluctuation of the potential barrier. Defects in the GBs—like facets, atomic steps and secondary grain boundary dislocations—which are characteristic of both boundaries can act as nuclei to the impurity segregation.

1 Introduction

The great interest in the atomic structure of grain boundaries (GBs) is based both on the practical application of polycrystalline semiconducting materials and on the fundamental aspect of the relationship between their physical properties and structures [1–3]. For most of the tilt GBs EBIC, DLTS and capacitance measurements were found to demonstrate similar features so that there had been no evidence of a correlation between the intrinsic GB structure and the electronic properties [2]. Consequently, the latter should be attributed to extrinsic processes like point defect agglomerations and/or segregations of impurities. Nevertheless, the intrinsic atomic structure influences the point defect agglomerations so that further investigations will be necessary to substantiate these conclusions. During the last years many experimental studies as well as calculations of the structures and energies of symmetrical [001] tilt GBs in silicon and germanium have been carried out [4–11], particularly in connection with 400 kV HREM (see Table 1). More than one stable, energetically relaxed structure has also been found for most of the grain boundaries [8–10]. The present paper describes TEM studies as well DLTS and steady state electrical measurements of Σ37(610) and Σ29(520) [001] tilt GBs in germanium, thus fulfilling two positions in Table 1.

2 Samples and Techniques

The germanium bicrystals were Czochralski-grown on double seeds. Bicrystals were mostly undoped, or doped with Sb at a concentration of 3×10^{-13} cm^{-3}. The dislocation density in their bulk was about 10^4 cm^{-2}. Two precisely oriented seeds (within 0.1 degree) were used. The starting material for the growth experiments was FZ germanium of high purity.

The bicrystals were cut into plates both perpendicular and inclined to the rotation axis [001], then they

*Presented at the Workshop on High-Voltage and High-Resolution Electron Microscopy, February 21–24, 1994, Stuttgart, Germany.

Table 1. [001] tilt grain boundaries in Ge (or Si) observed by TEM

GB plane $(k_1, k_2, 0)$	Σ	Θ (°)	CSL period d (nm)	α	$k_1/3k_2$	Reference
(910)	41	12.68	2.57	0.5	> 1	[10]
(710)	25	16.26	2.0	0.5	> 1	[10]
(610)	37	18.92	1.7	1	> 1	*
(510)	13	22.62	1.44	0.5	> 1	[10]
(310)	5	36.87	0.90	0.5	= 1	[5]
(520)	29	43.6	1.5	1	< 1	*
(320)	13	67.6	2.044	1	< 1	[8]
(11 3 0)	65	31	3.23	0.5	< 1	[8]

*Present paper

were mechanically polished on both sides and chemically thinned down to 100–150 μm. Circular disks of 3 mm in diameter were cut from the plates so that the boundary runs across their centres. Finally, the disks were thinned by means of chemical etching or ion milling until a hole appeared. JEM-7A (100 kV) and JEM-4000EX (400 kV) microscopes were used to determine the structure of the boundaries. The JEM-4000EX electron microscope (spherical aberration coefficient C_s = 1 mm) was equipped with a $\pm 15°$ goniometer stage. More than nine beams were used for imaging the atomic structure. Experimental images taken under different defocus conditions were analysed to deduce the geometrical structures present in the boundary core. Thus, several hypothetical structures were chosen to start computer calculations of relaxed models and the simulation of the HREM images using the CERIUS programme package [12]. A trial-and-error procedure [5] was applied to adjust simulated images to experimental ones.

Samples of $3 \times 3 \times 9$ mm^3 in size were prepared for electrical measurements so that the boundary passes through the centre of the 3×3 mm^2 face. Both types of samples were studied, i.e. those protected by wet-resistant lacquer to avoid surface ageing (I-type) as well as the unprotected (II-type) ones. Capacitance measurements and DLTS scans were performed over the temperature range of 70–300 K using a RF admittance bridge.

3 Geometrical Analysis of the Boundary Structure

From the geometrical point of view [6, 10] the majority of the boundary parameters can be deduced from a couple of integers (k_1, k_2) which completely describe the boundary geometry. Indeed, the normal to the boundary plane is $n_1 = [k_1, k_2, 0]$, the interface periodicity d_p is equal to $\alpha[-k_2, k_1, 0]$ and the Σ-value is equal to $\alpha(k_1^2 + k_2^2)$. The α-value is equal to 0.5 if k_1 and k_2 are odd and 1 otherwise. While the boundaries previously reported [5, 10] (see Table 1) have $\alpha = 0.5$, in the present paper α is equal to 1 for both boundary types.

According to the symmetry of diamond-like crystal lattices, the singular geometrical description requires the restriction on k_1 and k_2 value so that, e.g., $k_1 > k_2 > 0$. The value $k_1 = 3k_2$ corresponding to the $\Sigma 5(310)$ [001] grain boundary divides all [001] tilt boundaries into two domains (with $k_1 > 3k_2$ and $k_1 < 3k_2$) [10]. Most of the experimental results have been obtained for the first domain (see Table 1). In the present paper the $\Sigma 37(610)$ GB belongs to this ($k_1 > 3k_2$) while the $\Sigma 29(520)$ boundary belongs to the second domain ($k_1 < 3k_2$), and one can expect noticeable difference in their structures.

In accordance with the structural unit model [6–11], the boundary core can be represented either by a periodic sequence of a mixture of trigonal-pentagonal units (A or B), by distorted cubic (perfect) ones (p), or equally well by the cores of grain boundary dislocations (GBDs) with a Burgers vector of the type $1/2\langle 110\rangle$. In the notation of Rouviere and Bourret [10], A-units correspond to the core of edge dislocations while B-units correspond to 45° ones. Depending on the chirality and the orientation of these units 16 different dislocation cores were revealed [8–11], resulting in many possible variants for the boundary structure. For example, the decomposition of the GBD Burgers vector of $\langle 100\rangle$ type into two A- or B-units leads to a zigzag (Z) or symmetrical (S) boundary model, respectively, in addition to the ambiguities possible as a result of the rearrangement of bonds.

4 Electron Microscopy Study of Real Boundary Structure

The TEM studies show a real structure of the GBs which differs from the ideal structure described above by the presence of defects. The most important defects are facets and atomic steps on the boundary plane which are usually connected with the presence of lattice dislocations in the GB plane as well as secondary grain boundary dislocations related to the misorientation of the grains from the exact lattice coincidence.

The different bicrystals studied show various degrees of boundary plane faceting (see Figs. 1 and 2).

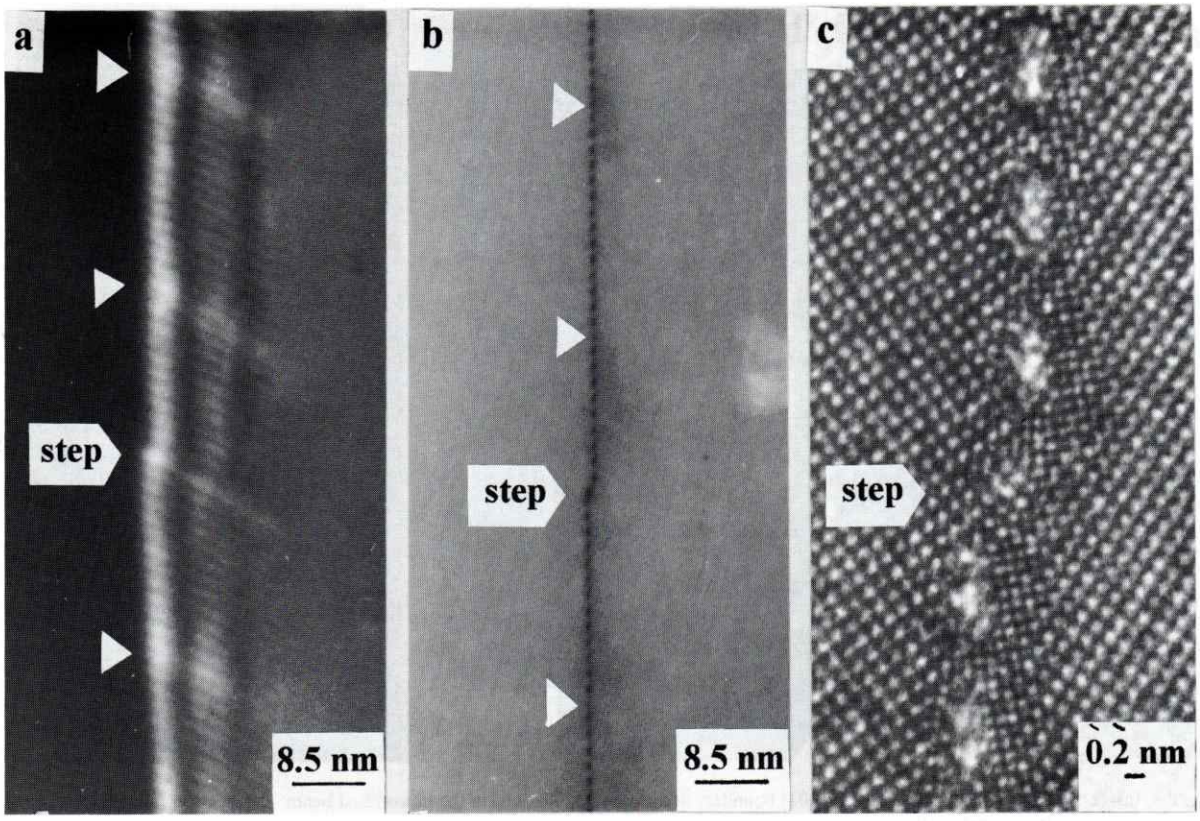

Fig. 1. (a)–(c): TEM images of the Σ37(610)/[001] grain boundary (weakly faceted) at different inclinations to the transmitted beam: bright field (BF) images of inclined GB (a) and GB in edge-on orientation (b), (c) – 400 kV-HREM image. The arrows indicate secondary GBDs.

Figure 1 shows micrographs typical of the weakly faceted boundary taken at different magnification and different inclinations to the transmitted beam. Both primary and secondary dislocations are revealed as rows of lines parallel to the tilt axis [001].

A faint oscillatory contrast in the inclined boundary plane is shown in Figure 1a. The secondary dislocations in the image are revealed as regions of brighter contrast, each at the place of two primary lines. The periods of the primary and secondary dislocation spacings are 1.7 nm and 15–25 nm, respectively. Figure 1b shows an image of the boundary in edge-on position. A sequence of black dots corresponds to the arrangement of primary dislocations in the GB. The secondary dislocations are localized inside some of these dots thus reducing their size (marked by arrows). The weak dark contrast appears at such dots due to the strain fields of the secondary dislocations located there.

The TEM images of Figs. 1–2 also show steps in the GB plane. Most of them exhibit a brighter contrast (Fig. 1a). HREM images show the presence of lattice dislocations at the steps (see, e.g., Fig. 1c).

It turned out that the surface of a strongly faceted boundary is corrugated consisting of a set of planar regions of 20 to 500 nm in extension, both symmetric and asymmetric. The latter are deflected from the symmetric position by an angle up to 20 degrees (Fig. 2a). Some of the boundaries consist of alternating asymmetric parts close to the $(100)_1//(310)_2$ orientation of the first grain related to the second one, and vice versa. According to the coincidence site lattice (CSL) for $\Sigma = 37$, these planes have a high density of atoms. In the plan-view image presented in Fig. 2b a strongly faceted boundary is shown as a terrace-like surface, which consists of planar regions separated by steps. The latter are fragments of both asymmetric tilt boundaries and twist ones. The fragment of a twist facet is shown in Fig. 2c.

Figure 3 shows typical images of the Σ29(520)/[001] GB for different orientations. While defects—

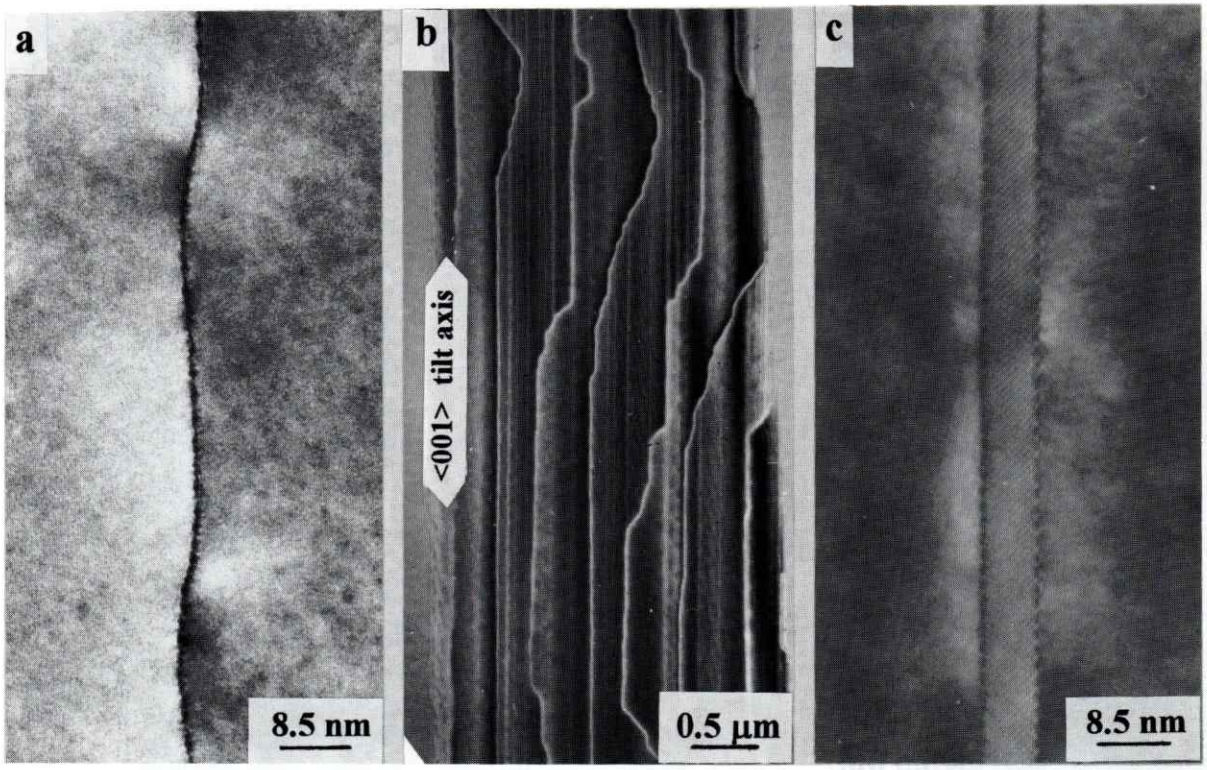

Fig. 2. (a)–(c): Strongly faceted Σ37(610)/[001] boundary at different inclinations to the transmitted beam: BF electron micrographs of the edge-on oriented GB (a), of the GB in nearly plan-view (b) and of a twist facet which is normal to the [001] tilt axis (c).

like facets, atomic steps, primary and secondary GBDs similar to Σ37(610) boundary type—have been observed, the real structures of the boundaries look rather different (one can compare, e.g., Figs. 1c and 3c). Indeed, a comparison of the atomic structures of Σ37(610) and Σ29(520)/[001] boundaries shown in Fig. 4 also confirms this conclusion.

Figures 4(a) and 4(d) demonstrate typical image-processed HREM micrographs of Σ37(610) and Σ29(520)/[001] boundaries, respectively. In the images, the very thin crystal regions near the hole were exposed where the crystal thickness did not exceed 300 Å. The exact thickness determination was rather difficult owing to the bending of the foil near the hole and morphology roughness at the boundary (groove effect) during the chemical etching. The typical thickness was approximately in the order of the extinction distance ξ_0 (=250 Å), i.e. in the range of 180–280 Å, because of foil stability under the beam. The defocus applied was about −70 nm in Fig. 4(a) and about −80 nm in Fig. 4(d). Here we rely on the convention that under-focus is negative whereas over-focus is positive. It was hard to determine the exact value of the under-focus to a high degree of accuracy because the amorphous edge of the specimen was slightly bent so that it could not be used for the correct defocus determination. The estimation of defoci was made using the amorphous rings presented in the digital diffractograms (see, e.g., inserts in Figs. 4(a) and (d)). The thickness and defocus values were also corrected during the matching of the simulated images to experimental ones described below. The above mentioned image processing has been applied to the micrographs in order to increase the contrast of boundary cores. The crystalline reflections (altogether 24) in the digital diffractograms (see inserts in Figs. 4(a) and (d)) of the experimental images were masked by small region filters (the image size usually was 1024 · 1024 pixels). The inverse Fourier transform provided the enhanced images (Figs. 4(a) and (d)), which differ from the original micrographs by the effect of scattering from the thin amorphous layer on the surface. Plane squared lattices were drawn for both grains to deduce the simple geometrical model of GBs and to determine their rigid

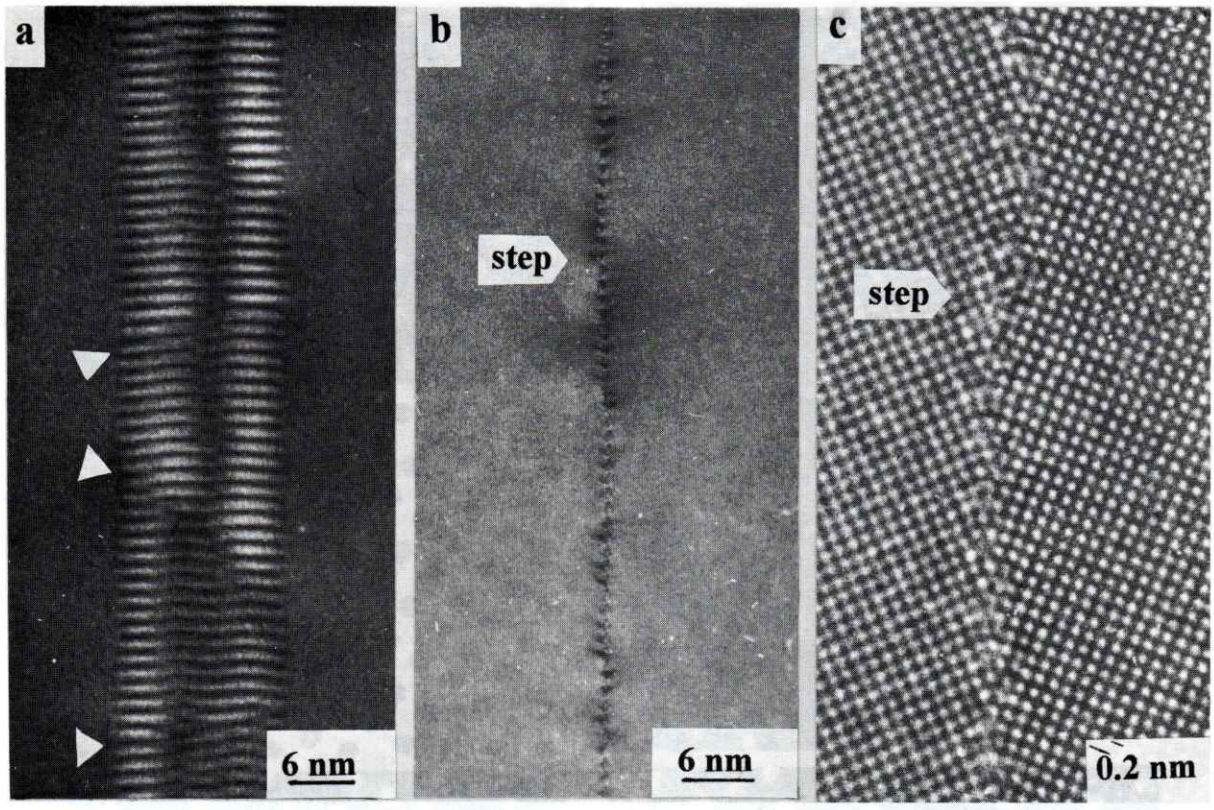

Fig. 3. (a)–(c): Electron micrographs of the Σ29(520)/[001] grain boundary at different inclinations to the transmitted beam: bright field (BF) images of inclined GB (a) and GB in edge-on orientation (b), (c)-400 kV-HREM image. The arrows indicate secondary GBDs.

body translation (RBT) in the image plane. A larger RBT value was found for the Σ29(520)/[001] boundary whereas the Σ37(610)/[001] boundary showed a relatively small RBT. Thus, the atomic structures of the GBs under consideration are rather different.

5 Image Simulation and Structure Modelling

The atomic models of the GBs were proved by interpreting HREM micrographs of different defoci. The models were then refined by means of a trial-and-error method applying alternatively the image simulation and the molecular static calculation of relaxed structures. The generation of GB models as well as image simulation were carried out by using the CERIUS programme package [12]. A certain combination of a Morse-type pair potential with an angular energy term, which was as close as possible to a modified Tersoff-pair potential [13], was chosen for the molecular static simulation of the structure relaxation of the initial geometrical model. Multislice image simulations (CERIUS program package, [12]) were performed for relaxed models in order to fit the calculated HREM images to the experimental ones. The corrections of the initial geometrical model were made based on the analysis of the difference between calculated and experimental images. This procedure was repeated to attain the best match of calculated images (Figs. 4(b) and e)) with the experimental ones (Figs. 4(a) and (d), respectively). The final results of the procedure were considered to be the most reliable models (Figs. 4(c) and (f)) with respect to the GB type, the crystal thickness and the image parameters. Comparing the boundary models of Figs. 4(c) and (f) reveals the difference in the atomic structures of the GBs under study, implying also different electronic properties of these types of GBs.

6 Electronic Properties of GBs

GBs of highest structural perfection (weakly faceted GBs) were selected for DLTS and other electrical

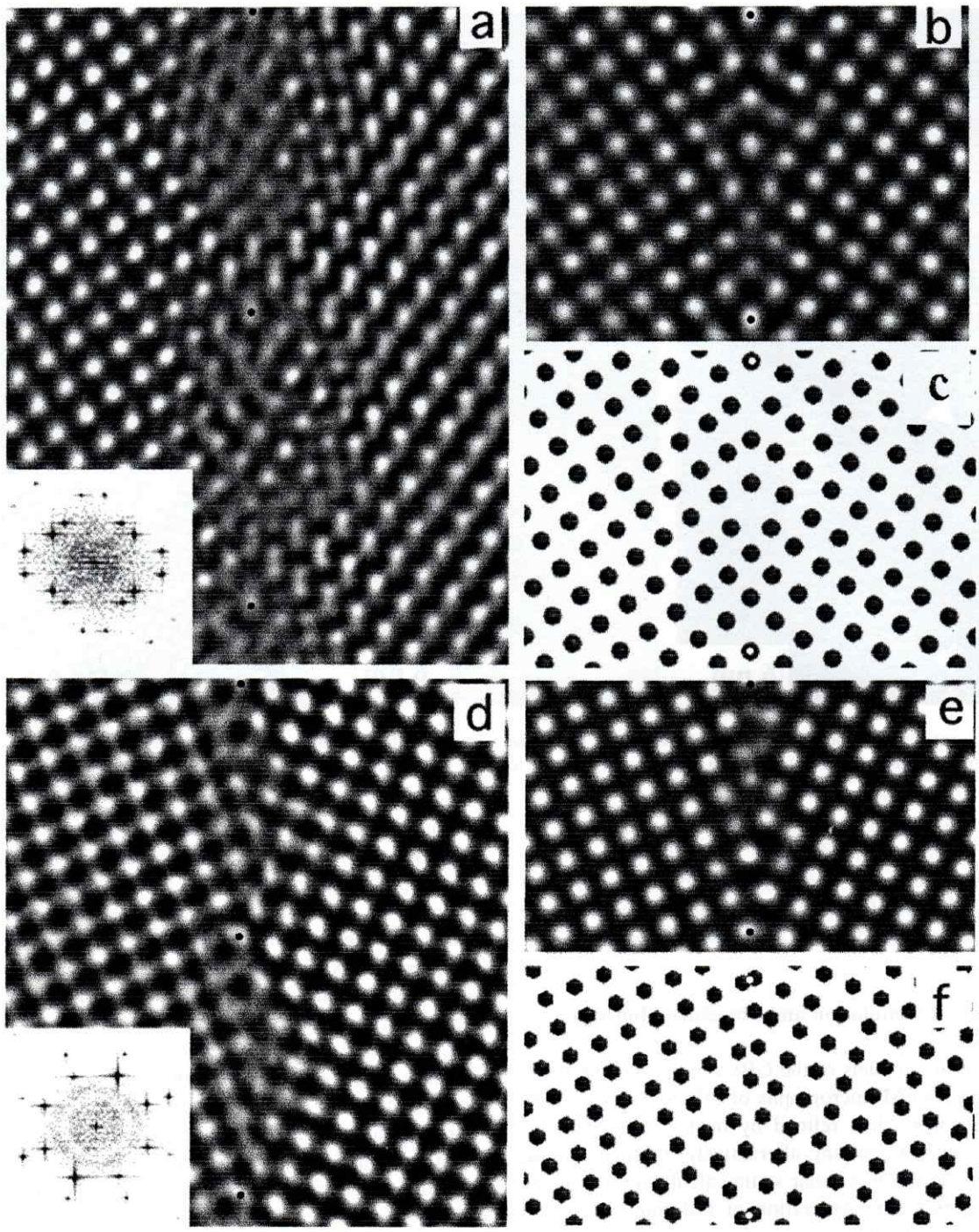

Fig. 4. (a)–(f): Image-processed HREM micrographs of $\Sigma 37(610)/[001]$ (a) and $\Sigma 29(520)/[001]$ (d) boundaries and corresponding computer simulated images ((b) and (e), respectively) which were calculated using the boundary models shown in (c) and (f), respectively. Reference points are marked in the images by small dark circulars. Original micrographs were taken at defoci δ_0 of -70 nm and -80 nm, respectively. Simulated images were calculated at the thickness t and defoci δ_0 in nm: 27.2 and -70 (b) 18.1 and -80 (e), respectively. Accelerated voltage $U = 400$ kV, spherical aberration coefficient $C_S = 1$ mm, beam spread $a_D = .5$ mrad, aperture size $a = 16$ nm^{-1}.

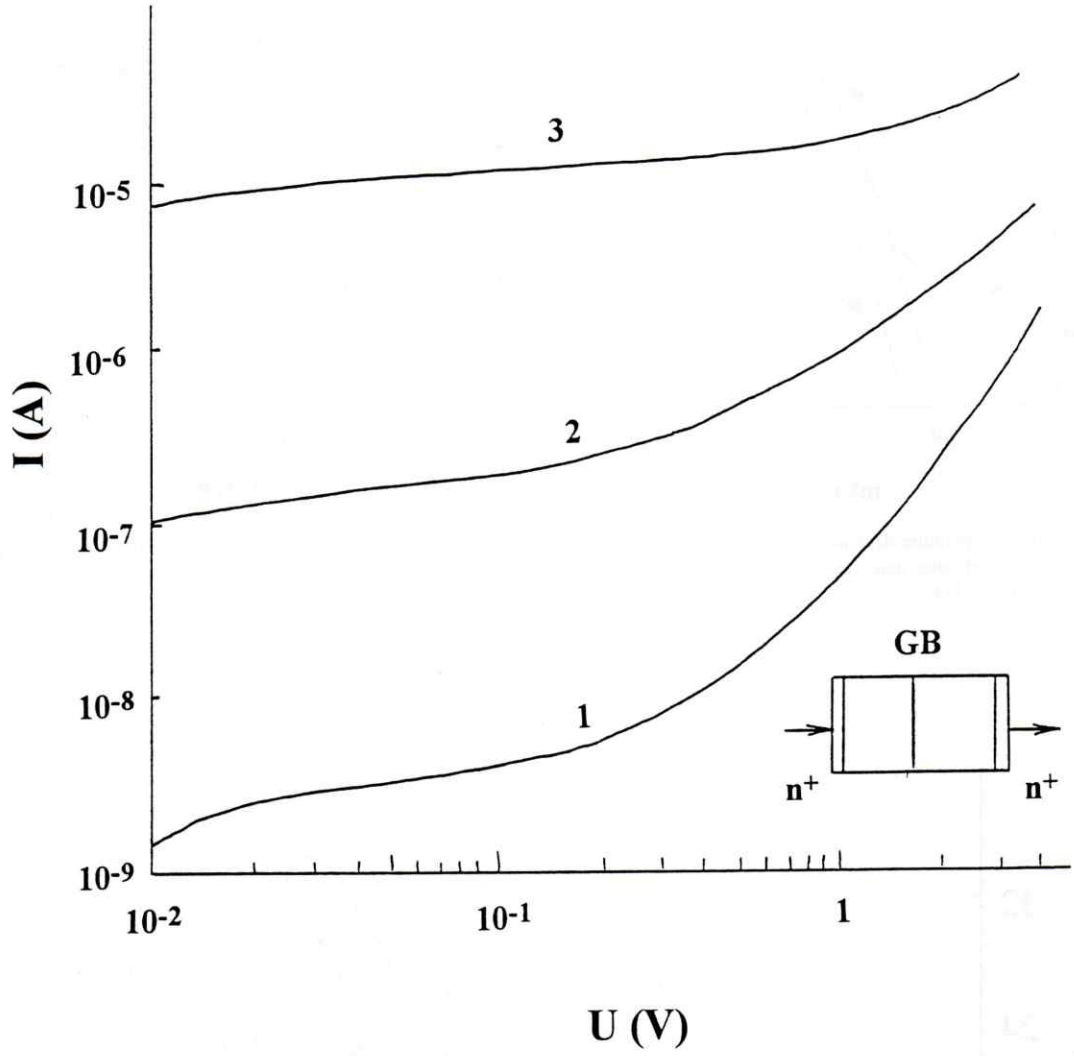

Fig. 5. Current-voltage (I-U) dependences of $\Sigma 37(610)/[001]$ GB (sample I) at various temperature, T in K: 208(1), 226(2), 252(3). Inserted is the sample scheme.

measurements. DLTS spectra and steady state electrical characteristics were found to show a similar behavior for both boundaries studied. The current-voltage (I-U) dependences close to room temperature exhibit a current structure for both current directions (Fig. 5). If the temperature is reduced, at low bias voltages (U) a sublinear increase of the current is observed changing to superlinear with increasing bias. Typical temperature dependences of the zero-bias resistance R' and the resistance R measured across the GB are shown in Fig. 6a. The activation energy derived from the Arrhenius plots in the temperature range of 230–300 K is 0.74 ± 0.05 eV for different samples. For $T < 230$ K, the activation energy decreases as it approaches 0.39 eV.

Figure 7 presents typical DLTS spectra. The spectra measured for a pulse amplitude of $U' > 0.3$ V are asymmetrically shaped peaks with a characteristically low-temperature tail. The temperature dependences of the capacitance recovery time constant derived from DLTS spectra are shown in Fig. 6b (corresponding curves are labelled by the same numeral). The relaxation is exponential only for a small pulse amplitude ($U' = 0.05$ V), with the corresponding activation

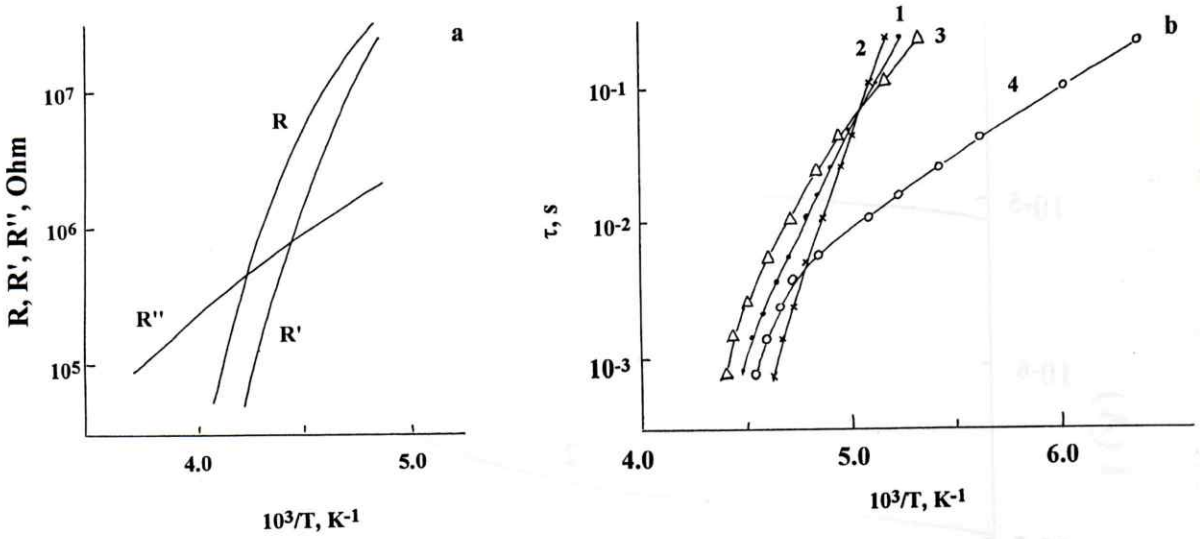

Fig. 6. (a–b): Temperature dependences of the zero-bias resistance $R'(U = 5$ mV), resistance R of $U = 0.5$ V, differential resistance R'' of $U = 1$ V(a), and capacitance recovery time constant (b) as derived from DLTS spectra in Fig. 7. Pulse amplitude, V: 0.051, (1, •); 0.3(2, ×); 0.6(3, Δ); 1(4, ○).

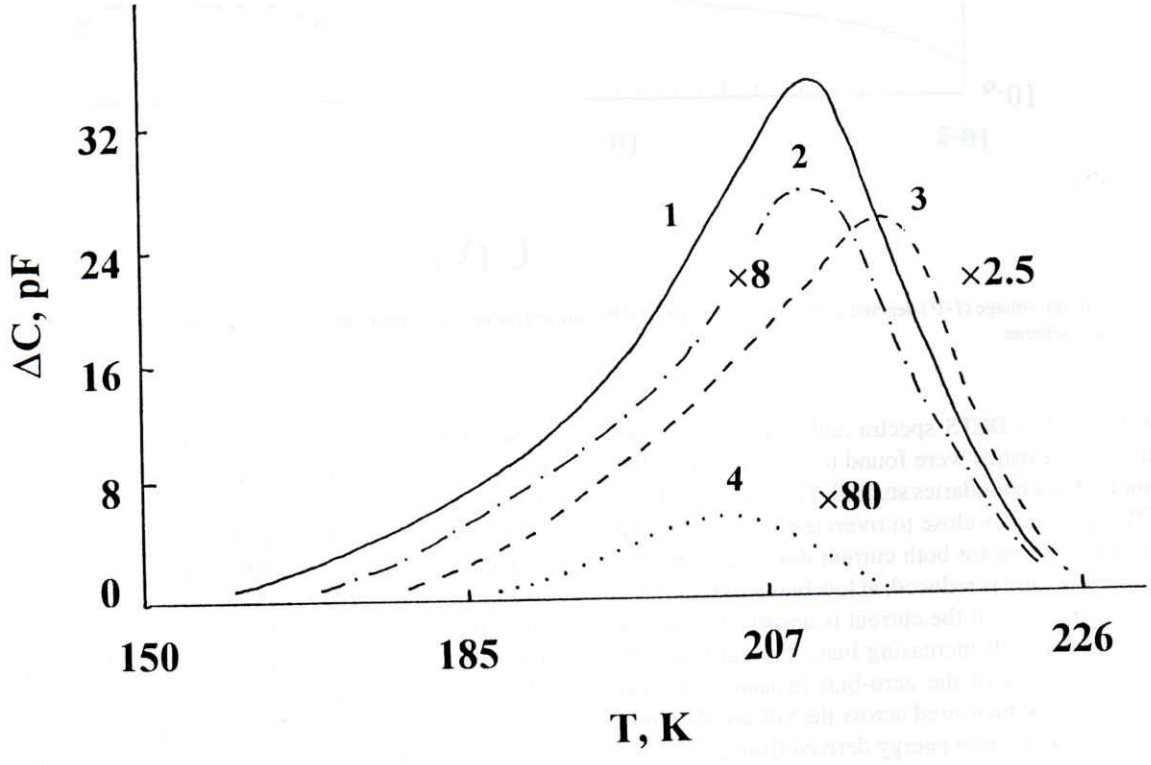

Fig. 7. DLTS spectra of the Σ37(610)/[001] GB. Frequency—150 kHz, rate window—5.16 ms, duration of pulse—1 ms, bias voltage $U = 0$, pulse amplitude, V: 0.05 (1, —); 0.3(2, — · —); 0.6(3,- - -); 1(4, · · ·).

energy being 0.74 ± 0.04 eV for different samples. There is a correlation between the slopes of the temperature dependences $\log R'$, $R(1/T)$ and $\log \tau(1/T)$. At low U', the values of τ and $R'C'$ are comparable, with $C' = 3 \cdot 10^{-10}$ pF being derived from the temperature dependence of the capacitance. There is also a correlation between the temperature shifts of these dependences as U and U' are increased. An increase of U' to 1 V results in a decrease down to 0.21 eV of the slope of the $\log \tau(1/T)$ dependence in the low-temperature part, which corresponds to the slope of the temperature dependence of the differential resistance $\log R''(1/T)$ measured at $U = 1$ V.

The equal values of τ and $R'C'$ allow one to suggest that the observed DLTS spectra are not associated with the thermal emission of charge carriers from the GB states to the band. They rather reflect the decay of the excess charge at the GB owing to the conduction current across the barriers on both sides of the GB when the voltage is dropped to zero. The observed activation energies of $0.74 + 0.04$ and 0.39 eV, which are close to the width of the forbidden gap E_g and $E_g/2$, are related to both the thermal generation of electron-hole pairs in the quasi-neutral and the depleted regions of the bicrystal. The activation energy of 0.21 eV is related to the "leakage" conductance across the boundary. In connection with DLTS measurements the equivalent circuit of the bicrystal can be represented in the form of two oppositely connected n-p-junctions shunted by a "leakage" conductance. For small U' values, the transition processes are determined by the value of $R'C'$, and for large ones, they are determined by the dependence on the voltage of each current component. One of the possible explanations for this are the GB barrier fluctuations owing to the spatial distribution of the point defects forming the regions with a high recombination activity. The activation-assisted conductance at the activation energy of 0.21 eV is associated with donor-like centres at E_c-0.21 eV belonging to vacancy-type oxygen complexes—their concentration correlating with the dislocation density [14]. This permits one to propose the following model of the potential barrier fluctuations arising at the boundary [15]. The position of the Fermi level at the boundary determining the barrier height is known to be close to the top of the valence band. It seems reasonable to assume that the donor states of the oxygen complexes in the GBs lead to a compensation as similarly happened for the boundary acceptor states, thus pinning the Fermi level near E_c-E_g/2-0.21/2, or E_c-0.21 eV.

7 Discussion

The atomic models of the Σ37(610) and Σ29(520)/[001] GBs are consistent with predictions of the modified structural unit model (SUM) [8, 10]. Using the SUM notation, the structure of the Σ37(610)/[001] boundary can be represented by various combinations of $(2A, 3p)$ or $(2B, 3p)$ units, or their mixture. The analysis of images of a weakly faceted boundary shows that the (B, p, B, p, p) sequence (S-type model) seems to be a better model than the Z-type one [11] as the first approach to the boundary structure. The S-type model is equivalent to the dissociation of the primary edge dislocation into two 45° partials.

The variations of the primary period from 1.7 to 1.45 nm have been observed in HREM images of Σ37(610)/[001] GB at the locations of secondary GBDs (every 10–15 primary periods for weakly faceted GB). Such variations of the primary period could also be described as local irregularities of the arrangement of structural units. While the basic period is equal to $d = a/2[610]$ the deviating one is equal to $d' = a/2[510]$, i.e. the latter corresponds to the Σ13(510)/[001] grain boundary. All primary dots are slightly elongated in a trace direction indicating the dissociation of the primary dislocations (see Fig. 1b).

A geometrical analysis predicts a $(3A, 2p)$ or a $(3B, 2p)$ sequence of structural units for the Σ29(520) boundary core. The present results show that the structure is more complex (see Fig. 4(f)) and the Z-type model is likely to be more probable, which is in contrast to the results of Rouviere and Bourret [10] where the S-model was found to be more reliable for the similar Σ13(320) GB.

While the Σ37(610) and Σ29(520) [001] tilt grain boundaries in Ge investigated in the present paper differ in their atomic structure, they show similarities in their electronic properties. The typical distance of secondary GBDs are found to correlate with the average charge spacings (~15–25 nm) deduced from the capacitance values. The excess conductance and capacitance of a bicrystal result from fluctuations of the potential barrier. The latter can be explained by the compensation of dislocation-related acceptor states by donor states of the oxygen complexes. Thus, obviously the effects of extrinsic boundary structure masks the intrinsic electronic properties of the GBs under consideration.

These conclusions concerning the Ge bicrystals are in good agreement with the previous results of Werner and Strunk [16] on Si bicrystals, pointing to the correlation between the charge sites within the grain boundary and the spatial distributions of secondary dislocations.

8 Conclusions

Grain boundaries in Ge bicrystals grown by the Czochralski method on a double seed have been investigated to elucidate the relationship between their atomic structure and electronic properties. Based on 400 kV HREM imaging and further image processing, the models of the boundaries under study have been deduced. The atomic models have been refined by means of a trial-and-error method [4] applying alternatively image simulations and molecular static calculations of relaxed structures, using the CERIUS programme package [12]. The structures of the $\Sigma 37(610)$ and $\Sigma 29(520)$ [001] tilt GBs have been found to be consistent with modified structural unit models and to be rather different for these two types of GBs.

DLTS data and steady state measurements were found to be quite similar for both GBs. The analysis of the DLTS spectra points to impurity segregation at the boundary and enables the explanation of the fluctuations in the potential barrier by the formation of vacancy-type oxygen complexes of a donor-like state at E_c-0.21 eV. Defects in the GBs like facets, atomic steps and secondary grain boundary dislocations (GBDs), which are characteristic of both boundaries, can act as nuclei to the impurity segregation. The typical distances of GBDs in both types of boundaries were found to correlate (the same order of magnitude) with average charge spacings deduced from the capacitance measurements. Thus, the present results give evidence of the extrinsic origin of localized deep states at the GBs.

Acknowledgment

The authors are thankful to Prof. W. Schröter, Prof. J. Thibault, Dr. R. Hillbrand, and Dr. O. Breitenstein for their interest in helpful discussions as to the present paper as well as to Prof. M. Lubalin for growing the Ge bicrystals.

References

1. C.H. Seager, G.E. Pike, and D.S. Ginley, *Phys. Rev. Lett.* **43**, 532 (1979).
2. A. Broniatowski and J.C. Bourgoin, *Phys. Rev. Lett.* **48**, 424 (1982).
3. N.I. Bochkareva, Yu. S. Lelikov, M.D. Lubalin, and Yu. G. Shreter, *Fiz. Techn. Poluprov.* **20**, 1396 (1986).
4. C.D'Anterroches and A. Bourret, *Phil. Mag.* A **49**, 783 (1984).
5. J.J. Bacmann, A.M. Papon, M. Petit, and G. Silvestre, *Phil. Mag.* A **51**, 697 (1985).
6. M. Kohayma, *Phys. Stat. Sol.* b **141**, 71 (1987).
7. A. Bourret, J.L. Rouviere, and J.M. Penisson, *Acta Cryst.* A **44**, 838 (1988).
8. A. Bourret and J.L. Rouviere, in: *Polycrystalline Semiconductors*, Eds. H.J. Möller, H.P. Strunk, and J.H. Werner (Springer-Verlag, Berlin, 1989) p. 8.
9. J.L. Rouviere and A. Bourret, *Ibid*, p. 19.
10. J.L. Rouviere and A. Bourret *J. Physique Coll.* **51**, C1-329 (1990).
11. A.A. Levi, D.A. Smith, and J.T. Wetzel, *J. Appl. Phys.* **69**, 2048 (1991).
12. CERIUS programme package, Molecular Dynamics Corp., 1993.
13. J. Tersoff, *Phys. Rev. Lett.* **56**, 632 (1986).
14. N.I. Bochkareva, *Sov. Phys. Sem.* **25**, 323 (1991).
15. N.I. Bochkareva, S. Ruvimov, R. Scholz, K. Scheerschmidt, and L.M. Sorokin, *Inst. Phys. Conf. Ser.* N134, 83 (1993).
16. J. Werner and H. Strunk, *J. Physique Coll.* **43**, C1-89 (1982).